Establishment and study of a polarized X-ray radiation facility*

Xing Zhou,[1,2] Xiao-Yu Qie,[2] Si-Ming Guo,[2,†] Yong-Bo Huang,[1,‡] Zi-Yao Shu,[2] Shi-Kui Huang,[2] Li-Peng Fan,[2] Kai-Yue Guo,[2] Tao Yu,[2] and Jin-Jie Wu[2]

[1]*School of Physical Science and Technology, Guangxi University, Nanning 530004, China.*
[2]*National Institute of Metrology, Beijing 100029, China.*

With the advancement in X-ray astronomical detection technology, various celestial polarization detection projects have been initiated. To meet the calibration requirements of polarimeters on the ground, a polarized X-ray radiation facility was designed for this study. The design was based on the principle that X-rays incident at 45° on a crystal produce polarized X-rays, and a second crystal was used to measure the polarization of the X-rays produced by the facility after rotation. The effects of different diaphragm sizes on the degree of polarization were compared, and the facility produced X-rays with polarization degrees of up to 99.55±0.96% using LiF200 and LiF220 crystals. This result revealed that the polarization of incident X-rays is one of the factors affecting the diffraction efficiency of crystals. The replacement of different crystals can satisfy the calibration requirements of polarized X-ray detectors with more energy points in the energy range (4–10) keV. In the future, the facility should be placed in a vacuum environment to meet the calibration requirements at lower energies.

Keywords: Polarized X-rays, Polarimetry, Calibration, Bragg diffraction

chinaXiv:202307.00202v1

I. INTRODUCTION

Since the dawn of X-ray astronomy, a wide variety of detectors have been launched into space for astronomical observations and considerable progress has been made. The primary objects of X-ray astronomy are black holes, neutron stars, and hot interstellar gases. Research in this field is oriented toward physical processes under extreme conditions, such as very high densities and very strong magnetic and gravitational fields. To probe the fine structures of celestial bodies, researchers have turned their attention to the detection of polarized X-rays. For example, the detection of polarization angles provides a more precise idea of the region of X-ray emission, and X-ray polarization is the main method for inferring the direction of rotation of isolated electromagnetically silent pulsars. Only polarimetric measurements can directly detect magnetic fields and constrain the radiation-emission mechanism, particle acceleration, and source geometry [1]. The lack of advanced technology has prevented humans from performing highly sensitive polarized X-ray measurements. A polarization degree of 19% was measured for the Crab Nebula at 2.6 and 5.2 keV by the OSO-8 astronomical satellite in the 1970s [2]. For high-energy objects, obtaining an upper limit on the degree of polarization of only a few tenths of a percent cannot provide an effective physical constraint.

To effectively measure the polarization, next-generation X-ray polarization satellites are being actively developed worldwide. In 2018, the X-Calibur telescope, a balloon-borne pixelated cadmium zinc telluride detector (CZT), was launched in Antarctica. It was capable of observing polarized X-rays in the (15–50) keV energy band, based on the rule that the direction of X-ray scattering prefers the direction of polarization [3]. The POGO+ detector was also onboard the balloon, which measured polarized X-rays based on Compton scattering and detected hard X-rays up to 160 keV [4, 5]. The next generation of balloon telescopes, XL-Calibur, is also being designed and is expected to be more sensitive than X-Calibur [6]. In 2018, China's PolarLight satellite was successfully launched. It carried a gas pixel detector (GPD) capable of efficiently performing photoelectron detection on a two-dimensional surface [7]. In 2020, PolarLight, for the first time, discovered the change in polarization during the sudden rotation and recovery of a pulsar, suggesting that the pulsar's magnetic field changed during this process [8]. In December 2022, NASA published the results of a study that found 60% high linear polarization in the outer regions of the Vela pulsar wind nebula (PWN) and observed X-rays in the interior of the nebula, whose polarization exceeded 60% at the leading edge and near the limit of synchrotron radiation [9]. This was a major breakthrough in astronomical observations [10]. The enhanced X-ray Timing and Polarimetry Mission (eXTP), a Chinese-led space exploration project, is expected to be launched in 2027 [11]. The detection targets of eXTP mainly include isolated and double neutron star systems, and strong magnetic field systems, such as magnetars, stellar masses, and supermassive black holes. The payloads of eXTP include the Spectroscopic Focusing Array (SFA), Polarimetry Focusing Array (PFA), Large Area Detector (LAD), and Wide Field Monitor (WFM). The PFA uses a gas pixel detector capable of detecting polarized X-rays at (2–10) keV [12]. In addition, a new astronomical satellite is expected to be launched in 2030, called the Chasing All Transients Constellation Hunters Space Mission (CATCH) [13]. The CATCH team plans to design three different detectors for time-varying spectral imaging and polarization detection with a polarization detector using a GPD with a sensitive energy of (2–8) keV.

Before a detector is launched, it must be calibrated on the ground so that it can accurately describe whether the de-

* This research was supported by the National Natural Science Foundation of China (No. 12205289).

† Si-Ming Guo, gsm@nim.ac.cn
‡ Yong-Bo Huang, huangyb@gxu.edu.cn

tected photons are linearly polarized or unpolarized. During irradiation by linearly polarized X-rays of different energies, the calibration of a polarization detector requires the amplitude of the detector response, also known as the modulation factor. This requires the construction of a facility to calibrate X-ray polarization. Currently, the most desirable polarized X-rays can be produced by synchrotron radiation devices; however, many polarized detectors require long calibration times to verify their stability. Moreover, the high cost of using synchrotron radiation devices makes them inconvenient as detectors for calibration [14, 15]. Bragg diffraction has therefore become an ideal option because it can provide monochromatic and linearly polarized X-rays. Previously, the National Institute of Metrology of China (NIM) was able to obtain monochromatic X-rays of (0.218–301) keV via Bragg diffraction and successfully calibrated satellite detectors for astronomical projects such as GECAM and SVOM [16–19]. In this study, we built a crystal diffraction-based polarized X-ray generation and verification facility to generate X-rays and verify that they are polarized.

chinaXiv:202307.00202v1

II. METHODS AND EXPERIMENTAL SETUP

A. Theory of polarization X-ray

During photon propagation, the electric and magnetic vectors are always perpendicular to the direction of propagation. In the plane perpendicular to the direction of propagation, the electric vector can be decomposed to form two components on the X and Y axes, which are simple harmonic vibrations along the X and Y axes. If the phase difference between the two components is 0 or 2π, then the direction of the electric vector is a straight line in the plane, at which point we call it linearly polarized.

X-rays are essentially photons in a specific wavelength range. X-rays incident on the surface of a crystal with neatly arranged atoms undergo Bragg diffraction according to Bragg's law [20]. This is shown by the fact that X-rays are reflected by the crystal in the same way as visible light is reflected by a mirror, and the reflected X-rays interfere when they satisfy the optical range difference relation. Thus, X-rays of different energies are distributed at different angles, with the distribution pattern shown in Equation 1.

$$2dsin\theta = n\lambda \tag{1}$$

where d is the lattice spacing of the crystal, n is the diffraction series, which can only be an integer, θ is the Bragg angle, and λ is the X-ray wavelength. After undergoing Bragg diffraction, the intensity of the diffracted X-rays is related to the angle θ. The integral reflection efficiency is defined as follows:

$$R_\lambda = \int_0^{\frac{\pi}{2}} P_\lambda(\theta)d\theta \tag{2}$$

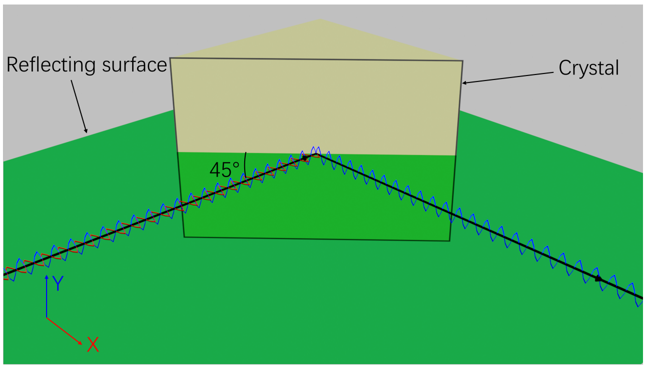

Fig. 1. Diagram of polarization when X-rays are incident on a crystal at 45°. The output X-rays only retain the y-component perpendicular to the reflecting surface; hence, they become linearly polarized X-rays.

Here, $P_\lambda(\theta)$ is the intensity of a unit intensity monochromatic X-ray diffracted by the Bragg angle θ. λ refers to the wavelength of the photon; for a fixed λ, the energy of the photon is fixed. The integral reflection efficiency R_λ is related to the polarization direction of incident X-rays. We can divide the direction of polarization of the X-rays incident on the crystal into two components, parallel to the direction of the reflecting surface (x-component) and perpendicular to the direction of the reflecting surface (y-component), according to the reflecting surface, as shown in Fig. 1, defining the ratio of reflectivity k:

$$k = \frac{R_\lambda^x}{R_\lambda^y} \tag{3}$$

k is the ratio of the reflection efficiency of the two components, and when $k < 1$, the polarization degree P can be expressed as in Equation 4:

$$P = \frac{1-k}{1+k} \tag{4}$$

Brewster's law followed by photons reflected from the interface of two different media is

$$\theta_B = arctan\frac{n_1}{n_2} \tag{5}$$

where n_1 and n_2 represent the refractive indices of the two media, and θ_B represents the Brewster angle. The refractive indices of different media satisfy the dispersion relation when photons propagate in the media [21]:

$$n = 1 + \frac{Ne^2}{2\epsilon_0 m}\frac{\omega_0^2 - \omega^2}{(\omega_0^2-\omega^2)^2+\omega^2\Gamma^2} \tag{6}$$

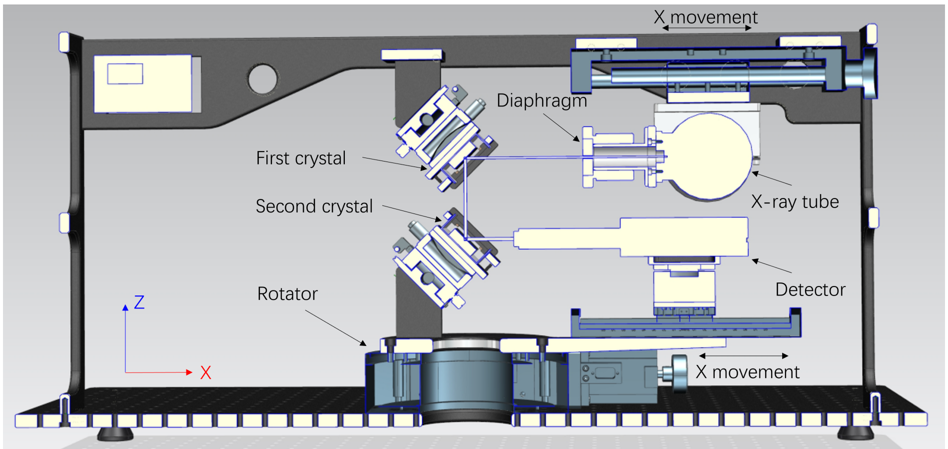

(a)

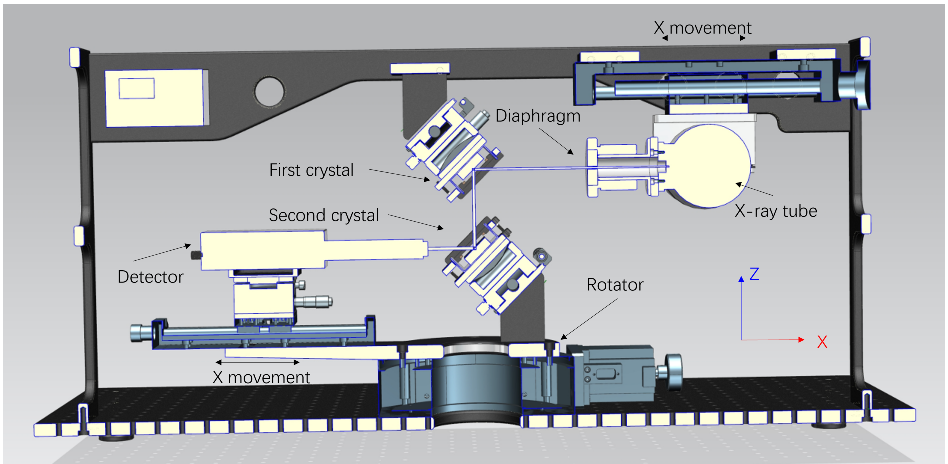

(b)

Fig. 2. Diagram of the polarized x-ray radiation facility. The X-ray tube and first crystal are fixed, and the second crystal and detector are placed on a turntable. The axis of the turntable passes through the center of the two crystals along the Z axis. Both the X-ray tube and detector can move along the X-axis. The X-rays generated from the X-ray tube are then diffracted by the first and second crystals at an angle of 45° and finally collected by the detector. Here, (a) is the facility in the 0° position, and (b) is the case when the turntable rotates to the 180° position.

chinaXiv:202307.00202v1

where m is the mass of the medium, N is the number density of the particles, and Γ is the amount of damping to which the electron vibration is subjected. ω_0 is the intrinsic frequency of the medium, ω is the photon frequency, and ϵ_0 is the vacuum dielectric constant. For X-rays, the wavelength of photons is considerably smaller than that of visible light, that is, the frequency is considerably larger than that of visible light; therefore, we can consider that $\lim_{\omega \to \infty} n$, and at this time, in either air or crystal, the refractive index n is close to 1. As a result, X-rays for each crystal Brewster angle are near 45° with this angle of incidence, $k = 0$ in Equation 4. As shown in Fig. 1, the x-component originally parallel to the reflecting surface disappears after reflection, and the output X-rays retain only the y-component perpendicular to the reflecting surface; thus, they become linearly polarized [22]. Hence, 45° was used as the starting angle for polarization in this experiment.

B. Studies of polarization X-ray facilities

Over the last century, crystals have been used to produce polarized X-rays. In 1963, researchers used topaz as a reflective material and detected the reflected X-rays at different incident angles [23]. As a result, the reflected X-rays reached their lowest light intensity at 45°, which is believed to be related to the polarization of the X-rays. In 1976, a similar study was conducted and applied to an OSO-8 polarization detector [2]. In 2021, another research team published a study that used a sheet of acrylic resin ($C_5O_2H_8$) as the reflective material to produce polarized X-rays with an incidence of 45° [24]. The polarization of the generated X-rays was examined using another sheet of the same resin, and the final polarization modulation curve was obtained; however, the degree of polarization was unsatisfactory. This was because parts of their facility were close together, resulting in a num-

Table 1. Measurement results of various crystals under 45° diffraction. In this table, the lattice spacing is the distance between the crystal faces within the crystal, in units of angstroms, which was calculated using the lattice constant and Miller index. The X-ray energy and count rate diffracted by each crystal at an incidence of 45° were measured using a silicon drift detector and the single crystal monochromatic X-ray beam facility [25].

Crystal	Lattice spacing (Å)	Energy (keV)	Count rate
LiF420	0.900	9.7	27
LiF200	2.013	4.3	446
LiF220	1.423	6.1	1799
Si511	1.089	8.4	32
Si551	0.792	11.5	36
Si331	1.298	7.0	82
Si220	2.000	4.6	93

ber of spurious peaks in the final energy spectrum, which affected the detection results. However, a large distance leads to the absorption of the low-energy part of the X-rays by air. In our design, the above experiences were referred to and helped make improvements.

C. Design of the polarization X-ray facility

The polarimetric sensitivity of polarization detectors in current astronomical observation projects is in the energy range (2–10) keV. It can be calculated using Equation. 1 that many Bragg crystals diffract at 45°, with the 1st diffraction energy within this energy band. We tested different crystals using the monochromatic X-ray facility at NIM, resulting in the data in Table 1. Although, theoretically, unpolarized X-rays can be diffracted through the crystal at an angle of 45° to yield linearly polarized X-rays, we must also examine the outgoing X-rays. The polarization and direction of polarization of the diffracted X-rays must be obtained.

In this study, we designed a polarized X-ray radiation apparatus based on the principle that X-rays incident at 45° on a crystal can produce linearly polarized X-rays, which was set up at NIM.

The X-ray machine shown in Fig. 2 was purchased from Keyway Electronics (model KYW2000B water-cooled). The power was 50 W, the current range was (0–1.5) mA, and the voltage range was (4–50) kV. The thickness of the beryllium window was 100μm, and the target material was silver. The tube after the beryllium window was filled with argon to avoid the absorption of X-rays by air. The first crystal was fixed to the crystal clamp above to ensure that the photons were incident at a 45° angle. The second crystal was fixed using the crystal clamp below. Two knobs on each crystal clamp were used to adjust the angle of the crystal to ensure that the X-rays were directed at center of the crystals. The same crystals were placed in both clamps during the experiment. The crystals used in this experiment were LiF200, with a lattice spacing of d = 2.013 Å, and LiF220 with a lattice spacing of d = 1.423 Å. According to the data shown in Table 1, the diffraction energies at a 45° incidence were 4.3 keV and 6.1 keV, and the diffraction monochromatic X-ray counts of LiF200 and LiF220 were higher than those of other crystals to meet the needs of this experiment. The silicon drift detector (SDD) shown in the figure and the second crystal were placed on a mechanical turntable. The turntable could be rotated by 360°, and its rotation could be controlled by software connected to a computer with a rotational accuracy of 10^{-4}°.

In the experiment, the X-ray tube first produced unpolarized X-rays that were emitted after passing through a beam-limiting diaphragm. After hitting the first crystal at an incident angle of 45°, the X-rays obtained by reflection diffraction were linearly polarized in the direction perpendicular to the paper surface. The X-rays from the first crystal hit the second crystal, where the turntable was at 0° and therefore did not change the direction of polarization, and were eventually reflected into the detector. After the 0° energy spectrum was collected, the turntable was rotated to record the energy spectra at other angles. After rotation, the reflecting surfaces of the two crystals formed an angle θ, and the final polarization detected by the detector was perpendicular to the reflecting surface of the second crystal. Ultimately, the intensity of the emitted X-rays varied with angle θ in accordance with Marius' law.

$$I = I_0 cos^2\theta \tag{7}$$

where I and I_0 are the outgoing and incident light intensities, respectively, and θ is the angle between the incident surfaces of the two crystals. After a 180° rotation, the facility stopped at the position shown in Fig. 2(b) and the reflecting surfaces of the two crystals coincided again. In our experiments, to

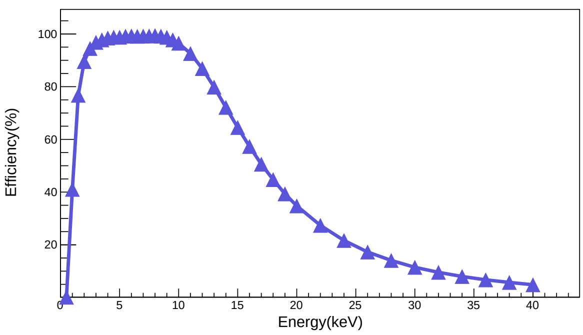

Fig. 3. Simulation results for detection efficiency of silicon drift detector.

consider the possible effect of the diaphragm aperture size on the polarization degree, we used 2 mm, 4 mm, and 6 mm aperture diaphragms for the following experiments, with the X-ray tube voltage set at 10 kV and a tube current of 0.95 mA. Because the period of the light-intensity transformation equation for Marius' law is π, the detector introduced additional background owing to the lack of shielding at the 180° position. Therefore, this experiment collected the count changes

chinaXiv:202307.00202v1

of the experimental setup over one cycle, with the angle θ varying from -90 to 90°, 5° for each rotation, and with each angle change collecting 60 s of energy spectrum data using the SDD.

D. Silicon drift detector

The SDD used in this study was previously used as a standard detector in a monochromatic X-ray calibration facility, and it had a cylindrical detection-sensitive volume with an area of 20 mm^2 and a thickness of 450 μm. The thickness of the beryllium was 8 μm. The detection efficiency was studied using Geant4 Monte Carlo simulations and validated using the radioactive source ^{55}Fe [26, 27]. The X-ray energy of ^{55}Fe radiation is mainly 5.9 keV, and the FWHM of the SDD at this energy is better than 133 eV. The detection efficiency curves are presented in Figure 3. The simulations demonstrated that the detection efficiency of the SDD was excellent at 10 keV and decreased rapidly with increasing energy. Because this study aimed for soft X-ray polarization detection below 10 keV, the SDD was the best choice.

III. PERFORMANCE TEST AND RESULTS

A. Performance of the facility

When crystal diffraction was used to obtain polarized X-rays, the resulting monochromatic X-rays also satisfied Bragg's law, such that a specific monochromatic peak appeared in the energy spectrum when incident at 45° on the LiF200 crystal. Figure 4(a) shows the energy spectrum collected by the detector when the X-rays were incident on the LiF200 crystal at an angle of 45° using a 2-mm diaphragm and in the original position. The diffraction peak had an energy of 4.25 keV, 1202 counts per minute, and an energy resolution of 2.73%. Figure 4(c) shows the energy spectrum collected by the facility using a 4-mm diaphragm and in the original position, with 1597 counts per minute of diffraction peaks, an increase in counts relative to the 2-mm diaphragm, and an energy resolution of 2.78%. Figure 4(e) shows the energy spectrum of the device with a 6-mm diaphragm, a count of 1943 per minute, and an energy resolution of 2.71%. For LiF220 crystals, the counts were higher than those for LiF200. Count = 4890 per minute in Fig. 4(b); count = 5884 per minute in Fig. 4(d); count = 6144 per minute in Figure 4(f). The energy resolution was approximately 2.25% for all three diaphragm cases.

To calculate the degree of polarization that can be achieved by the facility, the relationship between the photon count and the azimuthal angle was analyzed, as shown by the green triangles in Figure 5. The horizontal coordinates of the figure are the azimuths of the turntable (and second crystal), and the vertical coordinates are the counts for 60 s. Figure 5(a) shows a comparison of the energy spectrum counts collected at different azimuthal angles when the facility used a 2-mm diaphragm, from which we can see that the SDD collected the most counts at an azimuthal angle of 0 (in the original position) and decreased as the angle increased to either side, reaching a minimum at 90°, where it was no longer possible to distinguish monochromatic peaks from the spectrum. Figure 5(b) shows the variation in the energy spectrum counts with azimuth for the 4-mm diaphragm, with a similar pattern to Figure 5(a), but with more counts.

$$N_p = a \cdot cos^2((\theta - b) \cdot \frac{\pi}{180}) + c \tag{8}$$

The purple lines in Fig. 5 are the curves fitted using Equation 8, which is a variation of Marius' law (Eq. 7). In Equation 8, parameter a is the amplitude of the modulation curve, parameter b is the phase, parameter c is the lowest point of the curve, and Np represents the counts [28]. The parameters obtained from the fit allowed for the calculation of the degree of polarization.

$$P = \frac{N_{pmax} - N_{pmin}}{N_{pmax} + N_{pmin}} = \frac{a}{a + 2c} \tag{9}$$

In Equation 9, N_{pmax} and N_{pmin} represent the count of the curves at the highest and lowest points, respectively. The three parameters were obtained by fitting the data for different diaphragms and crystals, and the polarization degrees calculated using Equation 9 are listed in Table 2. From Equation 9, we know that when parameter c is less than 0, the polarization will be greater than 100%, which is not in accordance with the definition of the polarization degree. Therefore, we considered these data a failure of fit and did not calculate the degree of polarization. From the data, it appears that the maximum degree of polarization was obtained with a 2-mm diaphragm when using LiF200 crystals. A possible explanation for this is that a larger diaphragm does not effectively shield the background, resulting in a lower measured degree of polarization. When using the LiF220 crystal, while the count and energy resolution were better than those with Li200, the uncertainty was considerably greater than that with the other crystal. Consequently, the change in count was more erratic when the azimuth was changed. This made it easy to produce results that did not fit the theory. The data obtained in this experiment with the 2-mm and 6-mm diaphragms did not allow the calculation of polarization, whereas a polarization degree of 99.55±0.96% was obtained with the 4-mm diaphragm, which is close to that of linearly polarized X-rays.

In addition, we performed Gaussian fitting of the energy spectra measured at each azimuthal angle. Because the energy spectra above the 80° angle could not be fitted effectively, we excluded these data. We selected the data for LiF200 2 mm and LiF220 4 mm. The changes in the mean and sigma values obtained by the fitting are shown in Fig. 5(c) and Fig. 5(d). As shown in these plots, the average energy of the X-rays tended to decrease as the azimuth angle changed in

chinaXiv:202307.00202v1

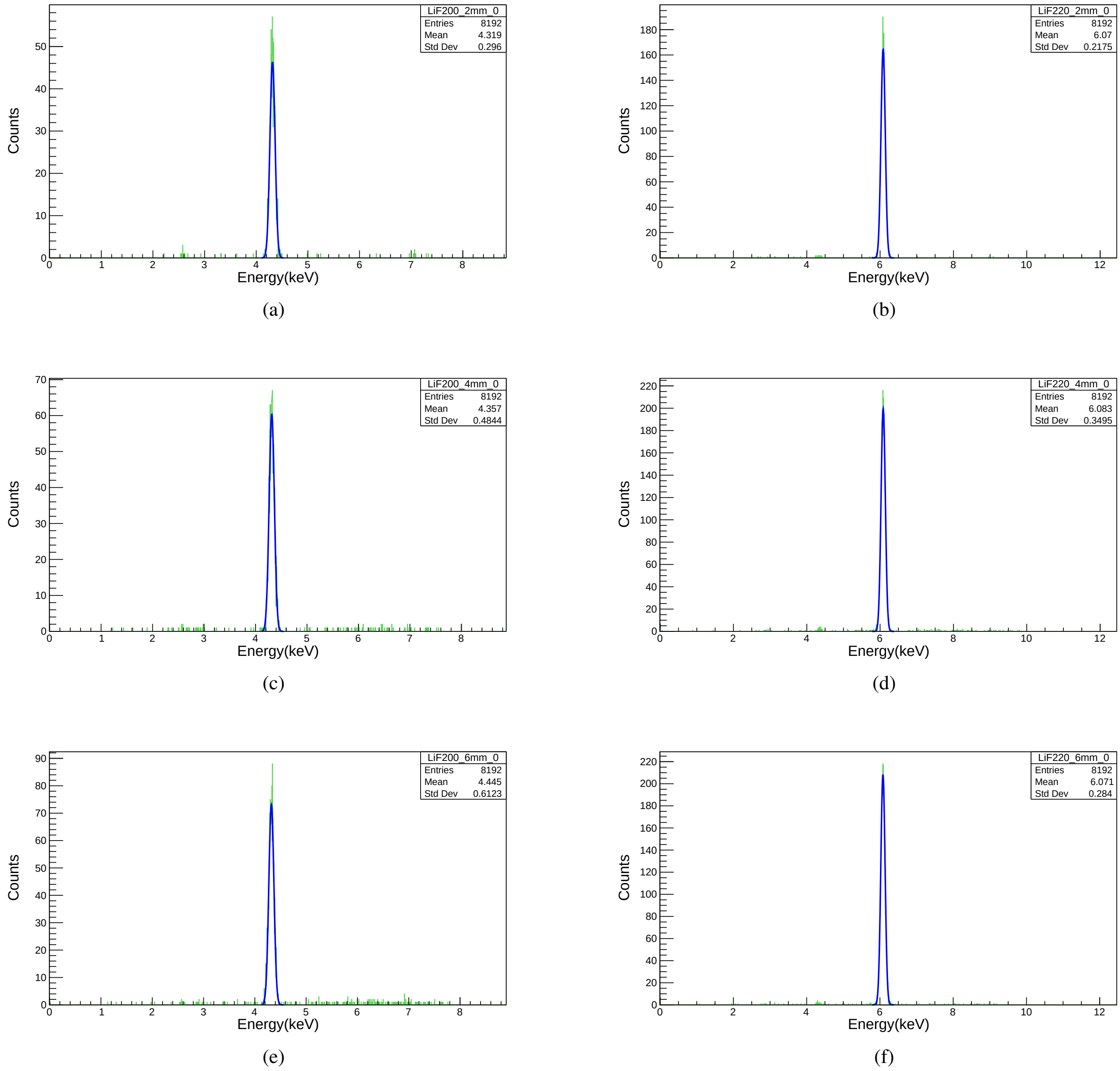

Fig. 4. Energy spectra detected by the SDD after diffraction of the LiF200 and LiF220 crystals. (a) and (b) correspond to the case using a 2-mm diaphragm, (c) and (d) correspond to the case using a 4-mm diaphragm, and (e) and (f) correspond to the case using a 6-mm diaphragm.(a), (c), and (e) are the energy spectra obtained using LiF200 crystals, whereas (b), (d), and (f) are obtained using LiF220 crystals.

the positive direction. This trend was even more pronounced in the case of the LiF220 crystals with a 4-mm diaphragm. A possible explanation for this trend is that, as the azimuthal angle increases, the Bragg angle of the X-rays to the crystal increases, resulting in a smaller diffraction energy. This suggests that the planes of the two crystals in the facility used in this study did not start out perpendicular but deviated somewhat. We compared the energy changes in the two different crystals and found that their energies tended to decrease as the azimuth increased. Therefore, we believe that the deviation originated from the facility itself rather than from the two crystals. In this facility, only the second crystal can be rotated; therefore, we assume that the angle of the clamp holding the second crystal is deviant. However, we currently do not have a sufficiently precise method to determine the angle between the two crystals, and this is where the study needs to be improved. If the angles of the two crystals are adjusted to the optimal position, the polarization can be higher than that at present.

In theory, the X-rays produced by the diffraction of X-rays through a crystal incident at an angle of 45° should be fully linearly polarized. However, in experiments, regardless of the narrowness of the diaphragm, it cannot completely filter out photons that do not exit in parallel. If the spot has a certain area, angular errors are introduced when diffracting from the crystal. This angular error also causes a reduction in polarization. When the polarization exceeds 99%, another physical quantity is required to describe the level of polarization: the

chinaXiv:202307.00202v1

Table 2. Fitting parameters and polarization degrees in different cases.

Crystal	Diaphragm size	Parameter a	Parameter b	Parameter c	Polarization degree (%)
LiF200	2 mm	1305.69 ±3.58	-1.29 ±0.08	20.70 ±1.14	96.21 ±0.16
LiF200	4 mm	1633.57 ±4.80	0.14 ±0.11	85.17 ±2.01	90.56 ±0.20
LiF200	6 mm	1737.65 ±3.34	-2.56 ±0.05	171.17 ±1.45	83.45 ±0.12
LiF220	2 mm	4931.74 ±64.61	-2.36 ±0.39	-107.5 ±39.03	/
LiF220	4 mm	5827.27 ±46.87	1.02 ±0.24	13.07 ±28.31	99.55 ±0.96
LiF220	6 mm	6032.84 ±41.22	1.27 ±0.21	-1.64 ±24.90	/

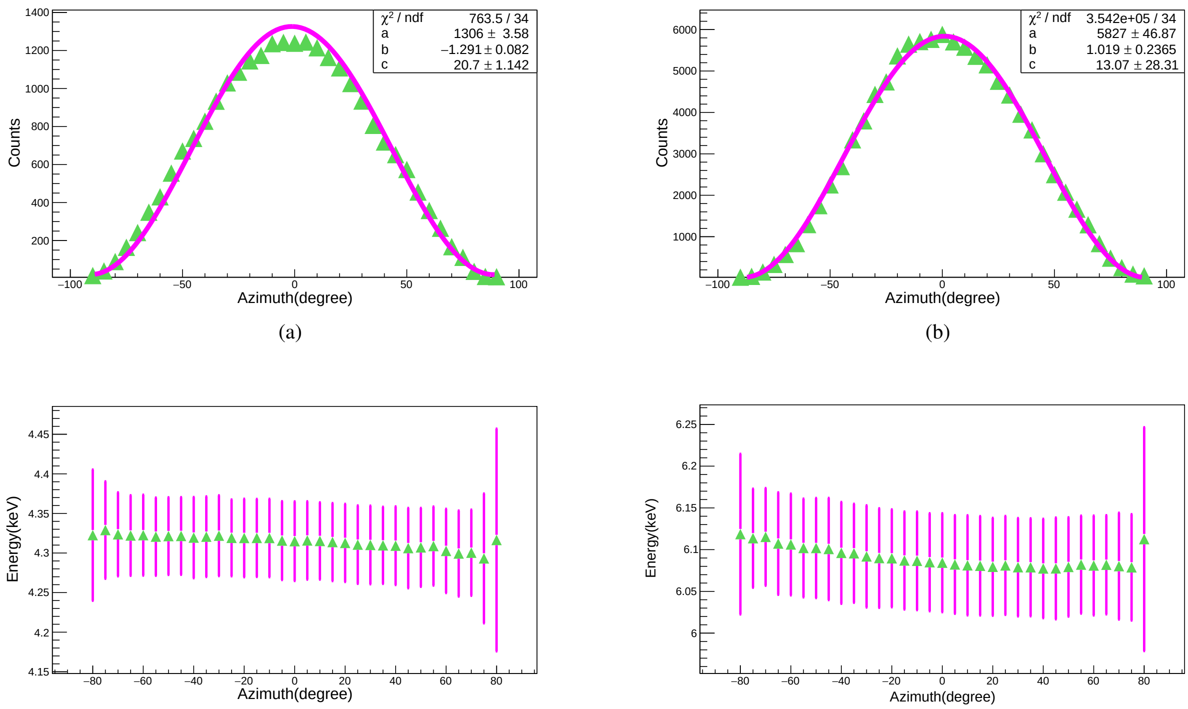

(a) (b) (c) (d)

Fig. 5. Azimuth measured during a 180° rotation of the turntable in relation to the detector counts and energies. (a) and (c) are for LiF200 with a 2-mm diaphragm, whereas(b) and (d) are for LiF220 with a 4-mm diaphragm.

chinaXiv:202307.00202v1

polarization purity, which is 1 minus the degree of polarization. One team used a processed channel-cut silicon crystal to create six consecutive 45° incidences and X-ray reflections within the crystal, ultimately achieving a polarization purity of 10^{-10} [29]. However, the X-ray source used by this team was a free-electron laser, which produces 10^{19} times the photon flux of an X-ray tube. The polarization was measured at test beamline ID06 at the European Synchrotron Radiation Facility. We did not consider this option because the free-electron laser facility is expensive and too large to meet the objectives of this study.

B. Simulation and future objectives

In the future, we will study X-ray-polarized sources in the energy range below 4 keV; however, X-rays in the lower energy range are easily absorbed by air. Polarized X-ray radiation facilities with energies below 4 keV cannot operate in air, and lower-energy photons must be properly detected in a vacuum environment [30]. At the same time, if the vacuum is too high, existing mechanical equipment will be rendered inoperable. To find a solution to this problem, simulations were performed using the open-source Monte Carlo simulation software Geant4. Considering that the optical path experienced by the facility in this study between the generation of X-rays and their detection by the SDD is approximately 30 cm, a length of 30 cm was chosen to simulate the transmission rate of X-rays at different air pressures. Based on a 2-mm diaphragm size, we set up a particle gun of 3.14 mm^2. The particles were oriented in the positive direction of the Z axis, and all objects were centered on the Z axis. A virtual detector with an area of 20 mm^2 and a thickness of 450 μm was placed at a distance of 30 cm along the same line as the particle gun. The purpose of this study was to simulate the detection of the SDD detector. When a photon enters, it is

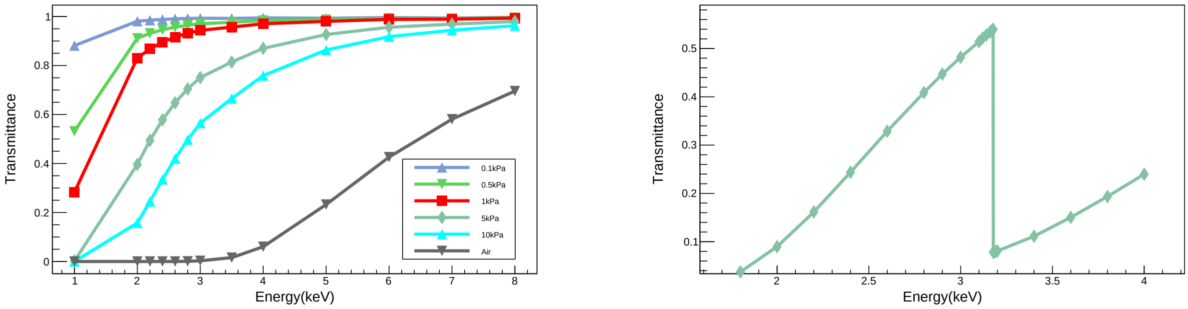

(a) (b)

Fig. 6. X-ray transmission rates at different air pressures at a 30-cm length simulated by Geant4.(a) No beryllium window.(b) With beryllium window and argon gas, but only air pressure of 1 kPa.

chinaXiv:202307.00202v1

judged whether it is able to pass through the gas. In this simulation, we set the air pressure to 0.1 kPa, 0.5, 1 kPa, 5 kPa, 10 kPa, and atmospheric pressure. The results are presented in Fig. 6(a). At 1 kPa, 1 keV photons could still be transmitted, and the existing facility could still be used, which is not particularly demanding in terms of confinement and therefore facilitates the connection of data and control cables.

Although photons below 4 keV can be transmitted in vacuum, at such low energies, a beryllium window becomes a mandatory consideration. Because the beryllium window of the X-ray tube was 100 μm thick and the beryllium window was filled with argon, they both had a high absorption of low-energy X-rays. Therefore, we performed Monte Carlo simulations again after considering these factors. We placed argon gas and the 100-μm-thick beryllium window between the particle gun and detector. The photon energy was set from 1.8 keV to 4 keV, and a 30-cm long vacuum at 1 kPa was set behind the beryllium window, with a virtual detector at the other end of the vacuum. The simulated transmittances are presented in Fig. 6(b). After considering the effects of the beryllium window and argon gas, the X-ray transmission rate was substantially reduced. Interestingly, at an energy of 3.2 keV, the X-rays exhibited a higher transmission rate. This is because argon has an absorption edge for photons at 3.2 keV. Photons at this energy were heavily absorbed by argon and produced a characteristic fluorescence of approximately 3 keV. We also observed high counts near 3 keV in the energy spectrum of the SDD during the experiment, even in air. However, in the energy range of (3.2–4) keV, there were almost no counts in the experiments in air, although there was a transmission rate of approximately 0.2 in a roughly vacuum environment. The same was true for the energy range of (2–2.5) keV. To solve the problem of count rates in these energy ranges, we will consider identifying materials that produce characteristic fluorescence at the corresponding energies in the future. To obtain the best diffraction results, the characteristic fluorescence energy of these materials should coincide with the 45° diffraction energy of the corresponding crystal.

IV. CONCLUSION

The facility built in this study was used to generate polarized X-rays and check their degree of polarization to confirm whether polarization calibration of the X-ray detector could be fully achieved. The effect of different diaphragm sizes on the performance of the generated X-rays in terms of monochromaticity and polarization degree was also tested, and it was found that the X-ray angular divergence had a certain effect on polarization. As clearly indicated by the results of this study, this facility is sufficiently good at producing polarized X-rays to meet the calibration needs of all types of polarized X-ray cosmic detectors at (4–10) keV after replacing the crystals. In addition, the diffraction efficiency of the crystal is also a worthy object of study. The present results indicate that the diffraction efficiency of the crystal may be affected by the degree of polarization and polarization angle of the incident photon.

The realization of the (4–10) keV polarization X-ray radiation facility is beneficial to the development of space astronomy in China. In the future, this facility can be retrofitted to provide polarization calibration services to eXTP, CATCH, and other polarization X-ray projects, enhancing China's international competitiveness in the field of space astronomy.

[1] P. Soffitta, N. Bucciantini, E. Churazov et al., A polarized view of the hot and violent universe. Exp. Astron. **51**(3), 1109-1141 (2021). https://doi.org/10.1007/s10686-021-09722-y

[2] M. C. Weisskopf, G. G. Cohen, H. L. Kestenbaum et al., Measurement of the X-ray polarization of the Crab Nebula. Astrophys. J. **208**, L125-L128 (1976). https://doi.org/10.1086/182247

[3] Q. Abarr, B. Beheshtipour, M. Beilicke et al., Performance of the X-Calibur Hard X-Ray Polarimetry Mission during its 2018/19 Long-Duration Balloon Flight. Astropart. Phys. **143**, 102749 (2022). https://doi.org/10.1016/j.astropartphys.2022.102749

[4] M. Chauvin, M. Friis, Jackson M, et al.: Calibration and performance studies of the balloon-borne hard X-ray polarimeter PoGO+. Nucl. Instrum. Meth. A **859**, 125-133 (2017). https://doi.org/10.1016/j.nima.2017.03.027

[5] M. Chauvin, H. G. Florén, M. Friis et al.: The PoGO+ view on crab off-pulse hard X-ray polarization. Monthly notes of the Royal Astronomical Society: Letters **477**(1), L45-L49 (2018). https://doi.org/10.1093/mnrasl/sly027

[6] Q. Abarr, H. Awaki, M.G. Baring et al., XL-Calibur–a second-generation balloon-borne hard X-ray polarimetry mission. Astropart. Phys. **126**, 102529 (2021). https://doi.org/10.1016/j.astropartphys.2020.102529 .

[7] E. Costa,P. Soffitta, R. Bellazzini et al.: An efficient photoelectric X-ray polarimeter for the study of black holes and neutron stars. Nature **411**(6838), 662-665 (2001). https://doi.org/10.1038/35079508

[8] H. Feng, H. Li, Long XY, et al.: Re-detection and a possible time variation of soft X-ray polarization from the crab. Nat. Astron. **4**(5), 511-516 (2020). https://doi.org/10.1038/s41550-020-1088-1

[9] F. Xie, A. D. Marco, F. L. Monaca et al., Vela pulsar wind nebula X-rays are polarized near the synchrotron limit. Nature **612**(7941), 658-660 (2022). https://doi.org/10.1038/s41586-022-05476-5

[10] V. Doroshenko, J. Poutanen, S. S. Tsygankov et al., Determination of X-ray pulsar geometry with IXPE polarimetry. Nat. Astron. **6**, 1433-1443 (2022). https://doi.org/10.1038/s41550-022-01799-5

[11] S. N. Zhang, A. Santangelo, M. Feroci et al., Enhanced X-ray Timing and Polarimetry mission—eXTP. Sci. China Phys. Mech. **62**, 1-25 (2019). https://doi.org/10.1007/s11433-018-9309-2

[12] S. N. Zhang, M. Hernanz, A. Santangelo et al., eXTP: Enhanced X-ray Timing and Polarization mission. Space Telescopes and Instrumentation 2016: Ultraviolet to Gamma Rays. **9905**, 505-520 (2017). https://doi.org/10.1117/12.2314582

[13] P. P. Li, Q. Q. Yin, Z. W. Li et al., CATCH: Chasing all transients constellation hunters' space mission. Exp. Astron. **55**, 447-486 (2023). https://doi.org/10.1007/s10686-022-09879-0

[14] F. Muleri, R. Piazzolla, A. D. Marco et al., IXPE Instrument Calibration Equipment. Astropart. Phys. **136**, 102658 (2022). https://doi.org/10.1016/j.astropartphys.2021.102658

[15] C. Feng H. X. Deng, Review of fully coherent free-electron lasers, Nucl. Sci. Tech. **29**, 160 (2018). https://doi.org/10.1007/s41365-018-0490-1

[16] S.M. Guo, Wu JJ,D.J. Hou. The development, performance, and applications of the monochromatic X-ray facilities in (0.218–301) keV at NIM, China. Nucl. Sci. Tech. **32**(6), 65 (2021). https://doi.org/10.1007/s41365-021-00890-2

[17] D. L. Zhang, X. Li, S. Xiong et al., Energy response of GECAM gamma-ray detector based on LaBr3: Ce and SiPM arrays. Nucl. Instrum. Meth. A **921**, 8-13 (2019). https://doi.org/10.1016/j.nima.2018.12.032

[18] D. Gotz, J. Paul, S. Basa et al., SVOM: A new mission for gamma-ray burst studies. Memorie Della Societa Astronomica Italiana Supplementi **21**(1), 162 (2009). https://doi.org/10.1063/1.3155898

[19] Y.W. Dong, B.B. Wu, Y.G. Li et al., SVOM gamma ray monitor. Sci. China Phys. Mech. **53**, 40-42 (2010). https://doi.org/10.1007/s11433-010-0011-7

[20] V. V. Aristov, A. I. Erko, A. Y. Nikulin et al., Observation of X-ray Bragg diffraction on the periodic surface relief of a perfect silicon crystal, Opt. Commun **58**(5), 300–302 (1986). https://doi.org/10.1016/0030-4018(86)90230-0

[21] A. Zangwill (eds.) *Modern Electrodynamics* (Cambridge University Press, Cambridge, 2012), p. 635 https://doi.org/10.1017/CBO9781139034777.

[22] F. Muleri, P. Soffitta, R. Bellazzini et al.: A very compact polarizer for X-ray polarimeter calibration. UV, X-ray, and Gamma-Ray Space Instrumentation for Astronomy XV **6686**, 296-307 (2007). https://doi.org/10.1117/12.734647

[23] Champion KP, R.N. Whittem, Utilization of increased sensitivity of X-ray fluorescence spectrometry due to polarization of the background radiation. Nature **199**(4898), 1082-1082 (1963). https://doi.org/10.1038/1991082a0

[24] N. Saito, R. Tanaka and J. Kawai, Polarization and intensity of Compton scattering. X-Ray Spectrometry **51**(1), 86-90 (2022). https://doi.org/10.1002/xrs.3261

[25] S.M. Guo, Z. Jiang, Wu J J, et al.: Research on a tunable monochromatic X-ray source in (5 $\sim$ 40) keV. Appl. Radiat. Isotopes. **181**, 110096 (2022). https://doi.org/10.1016/j.apradiso.2022.110096

[26] S.M. Guo, Wu JJ, J. Zhang et al.. Study on silicon drift detector efficiency using Monte–Carlo simulation and experimental methods. Journal of Engineering **2019**(23), 8543-8545 (2019). https://doi.org/10.1049/joe.2018.9051

[27] S. Agostinelli, J. Allison, K. Amako et al., Geant4—a Simulation Toolkit. Nucl. Instrum. Meth. A **506**(2003), 250-303 (2002). https://doi.org/10.1016/S0168-9002(03)01368-8

[28] F. Muleri, P. Soffitta, R. Bellazzini et al.: Gas pixel detector as an X-ray photoelectric polarimeter with a large field of view. Space Telescopes and Instrumentation 2008: Ultraviolet to Gamma Ray **7011**, 683-693 (2008). https://doi.org/10.1117/12.789621

[29] B. Max, K. S. Schulze, I. Uschmann et al., High-precision X-ray polarimetry. Phys. Rev. Lett. **110**(25), 254801-254801 (2013). https://doi.org/10.1103/PhysRevLett.110.254801

[30] M. Lemonnier, O. Collet, C. Depautex et al., High vacuum two-crystal soft X-ray monochromator. Nucl. Instrum. Meth. **152**, 109-111 (1978). https://doi.org/10.1016/0029-554x(78)90246-x

chinaXiv:202307.00202v1